Constraining global marine iron source and scavenging fluxes with GEOTRACES dissolved iron measurements in an ocean biogeochemical model

Christopher J. Somes[1], Andrew W. Dale[1], Klaus Wallmann[1], Florian Scholz[1], Wanxuan Yao[1], Andreas Oschlies[1], Juan Muglia[2], Andreas Schmittner[3], Eric P. Achterberg[1]

[1] GEOMAR Helmholtz Centre for Ocean Research Kiel, 24105 Kiel, Germany

[2] Centro para el Estudio de los Sistemas Marinos, CONICET, 2915 Boulevard Brown, U9120ACD, Puerto Madryn, Argentina

[3] College of Earth, Ocean, and Atmospheric Sciences, Oregon State University, Corvallis, Oregon 97331, USA

Corresponding author: Christopher J. Somes (csomes@geomar.de)

Key Points:

- Global marine iron model tests varying levels of atmospheric deposition, sedimentary release, ligand distributions and scavenging rates
- Simulations that best reproduce observations include variable ligands and high rates of atmospheric deposition and sedimentary release
- Simulations with high iron sources require high scavenging rates resulting in short residence times

Abstract

Iron is a key micronutrient controlling phytoplankton growth in vast regions of the global ocean. Despite its importance, uncertainties remain high regarding external iron source fluxes and internal cycling on a global scale. In this study, we used a global dissolved iron dataset, including GEOTRACES measurements, to constrain source and scavenging fluxes in the marine iron component of a global ocean biogeochemical model. Our model simulations tested three key uncertainties: source inputs of atmospheric soluble iron deposition (varying from 1.4 - 3.4 Gmol/yr), reductive sedimentary iron release (14 - 117 Gmol/yr), and compare a variable ligand parameterization to a constant distribution. In each simulation, scavenging rates were adjusted to reproduce the observed global mean iron inventory for consistency. The apparent oxygen utilization term in the variable ligand parameterization significantly improved the model-data misfit, suggesting that heterotrophic bacteria are an important source of ligands to the ocean. Model simulations containing high source fluxes of atmospheric soluble iron deposition (3.4 Gmol/yr) and reductive sedimentary iron release (114 Gmol/yr) further improved the model, which then required high scavenging rates to maintain the observed iron inventory in these high source scenarios. Our model-data analysis suggests that the global marine iron cycle operates with high source fluxes and high scavenging rates, resulting in relatively short surface and global ocean mean residence times of 0.83 and 7.5 years, respectively, which are on the low-end of previous model estimates. Model biases and uncertainties remain high and are discussed to help improve global marine iron cycle models.

1 Introduction

Iron is a critical micronutrient limiting primary productivity in vast ocean regions (Boyd and Ellwood, 2010;Tagliabue et al., 2017). Iron limitation is responsible for the development of so-called High Nitrate Low Chlorophyll (HNLC) regions of the Southern Ocean, Subarctic North Pacific, Subarctic North Atlantic, and Eastern Equatorial Pacific (Moore et al., 2013). Since dissolved iron (DFe) in the ocean exists in the picomolar (pM) to nanomolar (nM) concentration range, historical measurements with higher detection limits and contamination issues have hindered a robust global understanding of the marine iron cycle compared to macronutrients (Bruland et al., 2014). However, over the past two decades, in large part due to the GEOTRACES program, considerable progress has been made and reliable intercomparable iron

measurements have become available that permit a more synoptic view of the marine iron cycle (Schlitzer et al., 2018).

The increasing number of robust iron measurements has sparked recent modeling efforts. However, few observational constraints are provided on a global scale, and the degree of complexity and assumptions on the mechanistic processes implemented in global marine iron models have varied dramatically (e.g., Tagliabue et al. (2016)). For example, there is no consensus on the rates of key source fluxes to the ocean, particularly from atmospheric deposition (Anderson et al., 2016) and sedimentary release (e.g., Elrod et al. (2004); Dale et al. (2015)) that vary between 1.4 - 30 Gmol yr^{-1} and 0 - 194 Gmol yr^{-1}, respectively, in state-of-the-art marine iron models (Tagliabue et al., 2016) . Since uncertainties associated with scavenging and removal of DFe are also high, global marine iron models can tune scavenging rates to reproduce the global iron inventory with large ranges of sources fluxes (Frants et al., 2016).

Another key aspect of marine iron models is the representation of ligands which organically bind DFe and thereby prevent it from being scavenged to sinking particulates. Some models still prescribe a globally constant ligand concentration typically at 1 nM, while others account for ligand distributions via a parameterization or directly simulating ligands as a prognostic tracer. Ligands are thought to be produced by microbes as a by-product during the production of organic matter (Gledhill and Buck, 2012), including by heterotrophic siderophores that flourish when systems become iron stressed (Bundy et al., 2018). This has led modelers to predict ligand concentrations by assuming they are produced during the production of organic matter (e.g. Völker & Tagliabue (2015)) or by prescribing a relationship to other organic tracers such as dissolved organic matter and apparent oxygen utilization (e.g., Tagliabue & Völker (2011); Misumi et al. (2013); Pham and Ito (2018)).

The uncertainties associated with external source fluxes and scavenging represent key gaps in understanding the marine iron cycle. This hampers accurate estimates of the DFe budget, residence time and, consequently, its sensitivity to environmental perturbations and climate change. While the rapidly increasing amount of DFe measurements is improving our knowledge of the distribution and inventory of dissolved iron in the ocean, constraining external fluxes has proved to be more difficult. As a result, the range of residence times estimated by the current global marine iron cycle models ranges from less than a decade to multiple centuries (Tagliabue

et al., 2016), which limits our ability to confidently predict the impact of changes to the marine iron cycle on productivity in a future ocean. Observational estimates fall within a similar range (Johnson et al., 1997), noting that more recent studies estimate much shorter residence times in the upper ocean (~10 days - 4 years) (Croot et al., 2004;Sarthou et al., 2003) depending on the dynamics, iron pools considered, and source inputs in different regions (Black et al., 2020).

In this study, we use a global marine DFe dataset to constrain the iron cycle fluxes in a global marine biogeochemical model. We analyze model sensitivity simulations that focus on three key uncertainties: varying source fluxes of (1) atmospheric soluble iron deposition and (2) reductive sedimentary iron release, as well as the role of a (3) variable ligand distribution on DFe distribution and scavenging rates. The resulting DFe concentrations in each model simulation are evaluated against observations to determine the most realistic marine iron cycle fluxes among the model scenarios.

2 Model Description

We used the UVic Earth System Climate Model (Weaver et al., 2001) version 2.9 (Eby et al., 2009). In the following section, we provide a general overview of the model components then focus on improvements made to the marine iron cycle in this study, whereas other modifications applied to all model simulations are described in the supplementary information.

2.1 Physical Model

The physical ocean-atmosphere-sea ice model includes a three-dimensional (1.8x3.6°, 19 vertical levels) general circulation model of the ocean (Modular Ocean Model 2) with parameterizations such as diffusive mixing along and across isopycnals and eddy-induced tracer advection (Gent and McWilliams, 1990). The physical configuration is based on Somes et al. (2017) and includes parameterizations such as computation of tidally-induced diapycnal mixing over rough topography on the sub-grid scale (Schmittner and Egbert, 2014), anisotropic viscosity (Large et al., 2001;Somes et al., 2010), and enhanced zonal isopycnal mixing schemes in the tropics to better represent zonal equatorial undercurrents (Getzlaff and Dietze, 2013). A two-dimensional, single level energy-moisture balance atmosphere and a dynamic-thermodynamic sea ice model are used, forced with prescribed monthly climatological winds (Kalnay et al., 1996) and constant ice sheets (Peltier, 2004).

2.2 Marine Biogeochemical Model

The updated marine ecosystem-biogeochemical model coupled within the ocean circulation model is based on the Model of Ocean Biogeochemistry and Isotopes (MOBI), version 2.0. Briefly, MOBI includes three prognostic inorganic nutrient tracers (nitrate (NO_3), phosphate (PO_4), iron) and two organic (dissolved organic nitrogen (DON) and dissolved organic phosphorus (DOP)) phases, three phytoplankton (ordinary, N_2-fixing diazotrophs, calcifying coccolithophores), one zooplankton, sinking detritus (i.e. dead particulate organic matter (POM)), as well as dissolved oxygen (O_2), dissolved inorganic carbon, alkalinity, and $\Delta^{14}C$ (Figure S1). It combines latest features from previous studies focusing on the nitrogen cycle (Somes and Oschlies, 2015), iron cycle (Muglia et al., 2017), and carbon chemistry (Kvale et al., 2015). Note that MOBI also includes isotope systems of ^{13}C and ^{15}N (Schmittner and Somes, 2016), but they are not shown in this study focusing on the iron cycle. Our model experiments were simulated for over 5,000 years under pre-industrial boundary conditions as they approached their quasi steady-state.

2.3 Marine Iron Cycle Model

2.3.1 Base Configuration

The marine iron model configuration is based on previous UVic Kiel Marine Biogeochemistry Model (KMBM) (Nickelsen et al., 2015), including improvements implemented in Muglia et al. (2017) (Figure 1). The marine iron model includes explicit tracers for DFe and particulate iron (PFe). All phytoplankton grow with a constant elemental stoichiometry ratio of iron relative to nitrogen. The sources of DFe to the ocean are atmospheric soluble deposition (Luo et al., 2008), reductive dissolution and sedimentary release (Elrod et al., 2004;Moore and Braucher, 2008), and hydrothermal fluxes (Tagliabue et al., 2010) (Table 2, Figure 2). The ligand concentration determines the fraction of DFe that is organically complexed and thus unavailable for scavenging, whereas the remaining free DFe (DFe') pool can be scavenged to PFe. In the base simulation #1, ligands are prescribed to be globally constant at 1 nM as in previous iterations of the model. This simulation is given the name "*SedFeLow_LigConst*" to reflect its differences (i.e., low reductive sedimentary iron release and constant ligand distribution) from further changes made to the marine iron model in this study (see subsections below and Tables 1 and 2).

2.3.2 Scavenging

The general formulation for scavenging and partitioning of free and organically-complexed DFe remains unchanged from previous versions. Scavenging of DFe' to PFe occurs via two mechanisms in the model: (1) absorption onto particulate organic matter following (Honeyman et al., 1988;Parekh et al., 2004), which is a function of POM concentrations, DFe', and the particle scavenging rate; (2) inorganic scavenging, which depends only on DFe' and the inorganic scavenging rate following the scheme of Galbraith et al. (2010). This inorganic scavenging term primarily represents colloidal aggregation into larger, sinking particles as well as lithogenic scavenging not explicitly accounted for in our formulation. Here we use a non-linear formulation for inorganic scavenging following Galbraith et al. (2010) which was designed to account for high lithogenic scavenging rates to better reproduce DFe where atmospheric deposition is high (e.g., tropical and subtropical North Atlantic) (Pham and Ito, 2019;Ye and Völker, 2017).

In each model simulation, the scavenging rate parameters were tuned so that each simulation contains a nearly identical global iron inventory with an average global DFe concentration of 0.7±0.03 nM (Table 2). The inorganic scavenging term was adjusted to reproduce the iron inventory in the ocean interior since it is the dominant form of scavenging there, whereas the POM scavenging parameter was adjusted to the upper ocean DFe. The globally integrated rates of the different scavenging processes are shown in Table 2 and total basin-scale averages in Figure 4.

2.3.3 Ligand Parameterization

In the base model configuration (simulation #1 *SedFeLow_LigConst*), a constant ligand concentration of 1 nM is applied globally (see Table 1). However, the distribution of ligands in the ocean is variable (e.g. Völker and Tagliabue (2015)). Since iron-binding ligands are thought to be produced during the production of organic matter (Gledhill and Buck, 2012), dissolved organic matter (DOM) and apparent oxygen utilization (AOU) have been shown to qualitatively reflect some observed ligand concentration patterns (Misumi et al., 2013;Pham and Ito, 2018;Tagliabue and Völker, 2011). However, a first global model-data comparison with ligands simulated as prognostic tracers was less conclusive and is further complicated by large variations in binding strength of different types of ligands (Völker and Tagliabue, 2015). Therefore, to

maintain computational efficiency we pragmatically chose to implement a ligand concentration function rather than include additional prognostic tracers.

We implemented a variable ligand parameterization to estimate ligand concentrations based on a function of dissolved organic nitrogen (DON) and apparent oxygen utilization (AOU): $Ligand_{con} = \alpha \cdot AOU^{0.8} + \beta \cdot DON^{0.8}$, where α (0.015 nmol ligand/(mmol AOU m^{-3})$^{0.8}$) and β (0.21 nmol ligand/(mmol DON m^{-3})$^{0.8}$) are generic parameters that determine ligand concentration associated with the tracers AOU and DON, respectively. The parameters α and β were chosen so that the global ligand inventory remained at 1 nM consistent with *LigConst* simulations but now reflects changes in their spatial distribution (Figure 3). Model simulations with this variable ligand parameterization (simulations #2-5, see Table 1) have "*LigVar*" in their respective model simulation name.

Although we follow previous studies for the variable ligand parameterization (Misumi et al., 2013;Pham and Ito, 2018;Tagliabue and Völker, 2011), a few notable changes have been made in our version. Since AOU can be negative in the surface ocean due to dissolved oxygen supersaturation, we applied a minimum ligand concentration of 0.5 nM. Previous ligand parameterizations have also applied minimum ligand concentrations to account for ligands associated with more refractory forms of DOM not explicitly included in our model (Aumont et al., 2015;Tagliabue and Völker, 2011). We also applied an exponential parameter (0.8) to the AOU and DON terms, which reduces ligands associated to these tracers particularly when their concentrations are high. This helped the model from overestimating DFe concentrations when AOU and DON concentrations are at their highest concentrations in the model.

2.3.2 Reductive Sedimentary Iron Release Function

The base model version uses reductive sedimentary iron release based on the Moore and Braucher (2008) implementation of Elrod et al. (2004), $DFe_{sed} = \gamma_{FeSed} \cdot C_{ox}$, where the DFe flux from the sediments (DFe_{sed}) is determined by the sedimentary iron release rate (γ_{FeSed} = 0.27 μmol Fe mmol C_{ox}^{-1} m^{-2} d^{-1}), and organic carbon oxidation (C_{ox}) in the sediments. Note that the base model version uses the DFe flux rate from Nickelsen et al. (2015) that is lower than suggested by Elrod et al. (2004) (0.72 μmol Fe mmol C_{ox}^{-1} m^{-2} d^{-1}). Since this formulation yields lower global rates in the model compared with other implemented sedimentary functions

included in this study (described below), model simulations with this sedimentary iron function (#1-2) contain the name "*SedFeLow*".

We also implemented the sedimentary iron release function proposed by Dale et al. (2015), who compiled a global dataset of sedimentary DFe fluxes to constrain their model estimate. While it has a strong dependence on the flux of particulate organic matter to the seafloor, similar to Elrod et al. (2004), the dataset in Dale et al. (2015) also revealed a strong dependence on bottom water oxygen concentration. Dale et al. (2015) thus parameterized sedimentary DFe release as $DFe_{sed} = \gamma_{max} \cdot tanh(C_{ox}/bwO_2)$, where γ_{max} is the maximum flux under steady-state conditions, and bwO_2 is dissolved oxygen concentration in bottom waters interacting with the sediments.

We test two scenarios with the Dale et al. (2015) parameterization by altering the maximum flux under steady-state conditions parameter. The "*SedFeHigh*" simulations apply the value suggested by Dale et al. (2015) (γ_{max} = 170 μmol m^{-2} d^{-1}), whereas the "*SedFeMid*" simulation reduces the maximum steady-state flux value to 100 μmol m^{-2} d^{-1} to test more intermediate levels of sedimentary DFe release (see Tables 1 and 2). This reduced value was chosen to test a global sedimentary DFe flux approximately halfway in between *SedFeHigh* and *SedFeLow* since their fluxes differ by a large amount. Note that the *SedFeMid* simulation does not contain significant qualitative differences in its spatial distribution compared to *SedFeHigh.*

2.3.4 Atmospheric Soluble Iron Deposition

In the base configuration, we applied the atmospheric soluble iron deposition mask from Luo et al. (2008). It deposits 1.4 Gmol yr^{-1} of soluble iron to the global ocean, which is a low-end scenario compared to other estimates applied in the marine iron model intercomparison study (Tagliabue et al., 2016). This estimate from Luo et al. (2008) is one of the first deposition models that explicitly accounts for the soluble iron deposition rather than assuming a constant solubility percentage from total deposition.

Another scenario using the average flux from four recent atmospheric soluble iron deposition models has also been applied (Myriokefalitakis et al., 2018). The intermodel average global soluble deposition rate is 3.4 Gmol yr^{-1} with similar patterns as in Luo et al. (2008) but higher rates most notably in the North Atlantic (Figure 2). This simulation with high soluble

226 atmospheric iron deposition is only applied to the high sedimentary release scenario and is
227 therefore named "*Atm+SedFeHigh_LigVar*".

228 **3 Model Results and Data Comparison**

229 **3.1 Global Dissolved Iron Dataset**

230 The DFe database used in this study is a collection of observations from both
231 GEOTRACES Intermediate Data Product 2017 (7520 points; Schlitzer et al. (2018)) and prior
232 observations compiled by Tagliabue et al. (2012) (12371 points). Note that we excluded 37
233 measurements with high DFe concentrations (from 10 nM to 216 nM) mainly from locations
234 with high hydrothermal activities or near-shore settings, and thus the dataset contains
235 concentrations up to 10 nM. We then interpolated the database onto the UVic model grid for the
236 model-data comparison (Figures 3-6) and to calculate model-data statistical metrics (Figure 7),
237 which results in 5917 grid points covered with DFe observations.

238 Model-data misfit statistical metrics are sensitive to unresolved outlier concentrations and
239 spatial extent of the data interpolation onto the model grid. However, these aspects do not affect
240 which simulations best reproduce the global dataset according to statistical metrics. This is
241 illustrated by comparing metrics calculated from all observations (Figure 7 upper panels) to only
242 GEOTRACES (Figure 7 lower panels). The statistical metrics improve when using only
243 GEOTRACES observations (see differences in vertical axes ranges from upper and lower
244 panels), but the relative improvements in the model simulations are nearly identical. The
245 arbitrary threshold of 10 nM was chosen as a balance between including as many observations as
246 possible while still being able to calculate useful statistical metrics.

247 **3.2 Variable Ligand Distribution**

248 The simulation with constant ligands does not reproduce the major basin-scale features of
249 the observed DFe distribution despite that its globally averaged profile is (Figure 4b). Most
250 notably, simulations with constant ligands significantly overestimate the DFe in the interior
251 Southern Ocean (Figure 4k), a critical ocean basin for Fe-limited phytoplankton growth.
252 *LigConst* thus overestimates supply of DFe via upwelling, and underestimates Fe limitation of
253 phytoplankton growth, which is a key deficiency in the base configuration and previous model
254 versions (e.g. Muglia et al. (2017)).

255 The simulations with variable ligand concentrations (#2-5; *LigVar*) better reproduce the
256 ocean interior distribution of DFe. This is due to the AOU dependence of the variable ligand
257 parameterization which mainly determines ligand concentrations in the deep ocean since semi-
258 refractory DOM concentrations are low there in the model. This is most obvious when
259 comparing intermediate depths of the Southern and Indian-Pacific Oceans, which contain
260 relatively low and high values of AOU and thus ligand concentrations, respectively, according to
261 our parameterization (Figures 3,4). Lower ligand concentrations in the Southern Ocean enhances
262 scavenging causing lower DFe concentrations, with the opposite effect occurring in the Indian-
263 Pacific Ocean, and better reproduces observations in both basins. Therefore, the interior DFe
264 distribution with the variable ligand parameterization is better partitioned with respect to
265 observations (Figure 3) and improves the global model-data misfit (Figure 7).

266 The concentration of semi-refractory DOM largely determines ligand concentrations in
267 the surface ocean (Figure 3a). DOM concentrations are higher around the high productivity
268 regimes in the low latitudes with generally decreasing values towards higher latitudes (Somes
269 and Oschlies, 2015) (Figure S2). This pattern is reflected in the surface DFe distribution that
270 shows the same latitudinal trend in the variable ligand model (Figures 5). While this meridional
271 DFe pattern better reproduces low DFe concentrations in the HNLC Southern Ocean, it creates
272 larger model-data biases on high latitude continental shelves in the Bering Sea, Weddell Sea, and
273 European shelf seas (Figures 5a-d, 6b-d). This shows that while the overall variable ligand effect
274 significantly improves the global DFe distribution (Figure 7), model-data biases in some regions
275 (e.g. high latitude continental shelf seas) still increase.

276 **3.3 Sedimentary Iron Release**

277 The *SedFeLow* simulations provide a relatively poor fit to observed DFe concentrations
278 (Figure 7). They fail to reproduce the high DFe concentrations near continental margins (Figures
279 5, 6), suggesting higher sedimentary release rates are necessary to explain these features. The
280 simulated DFe distribution also lacks the strong spatial gradient towards depleted concentrations
281 in many open ocean regions in the observations. These overly smooth gradients in *SedFeLow* are
282 the result of low sedimentary release rates and low scavenging rates required to reproduce the
283 global mean DFe inventory, resulting in a relatively long global mean residence time of 35 years
284 among our simulations (Table 2).

The simulations with higher sedimentary release rates (Figure 2) produce higher DFe concentrations in continental shelf seas (Figures 5e-f, 6), particularly where bottom water oxygen is low in the low latitudes. The simulations applying high-end sedimentary Fe release rates (*SedFeHigh*) outperformed simulations assuming lower rates across all calculated statistical metrics (e.g., correlation coefficient, standard deviation, root-mean-squared error; see Figure 7)), with the intermediate release rate scenario *SedFeMid* performed between *SedFeLow* and *SedFeHigh*. Therefore, our model-data analysis suggests that high-end estimates for global reductive sedimentary iron release rates are the most realistic.

One region that was notably improved by high sedimentary release rates was the low latitude Pacific (Figure 5e-f, 6a). Observations there in both the eastern (near oxygen deficient zones (ODZs)) and western (Indonesian Shelf Seas) sectors show high DFe concentrations that are best reproduced in *SedFeHigh* scenarios. Since *SedFeHigh* simulations also contain high scavenging rates, they better reproduce the lowest DFe concentrations in the central locations between the continental margins as well.

The high DFe concentrations on high latitude continental shelf systems (Figures 5, 6b,d) are not significantly improved in *SedFeHigh* scenario due to the interactions with ligands and scavenging. Lower ligand concentrations in high latitude systems allow scavenging to compensate the additional sediment-derived DFe more efficiently, in contrast to low latitude systems (e.g. Tropical Pacific) that contain higher ligands and allow the DFe to be retained in the water column. Therefore, the model improves but still underestimates DFe in these high latitude continental shelf systems (e.g., Bering Sea and European Shelf Seas).

3.4 Atmospheric Soluble Deposition

The two soluble atmospheric deposition scenarios tested here predict similar spatial depositional patterns (Figure 2), with the more recent GESAMP intermodel average (Myriokefalitakis et al., 2018) providing a significantly higher global deposition rate (3.4 Gmol yr^{-1}) relative to the estimate from Luo et al. (2008) (1.4 Gmol yr^{-1}). These enhanced rates cause higher DFe concentrations mainly from the Saharan dust plume in subtropical North Atlantic, but also to a lesser degree in the Arabian Sea and North Pacific (Figure 5g,h, Figure 6d). The impact of including higher soluble deposition only slightly improves the global model-data statistical

metrics, making it difficult to judge the most realistic scenario based on our model-data DFe comparison alone.

3.5 High Scavenging Effect

In model simulations with high source fluxes (e.g. #5 *Atm+SedFeHigh_LigVar*), higher scavenging rates are necessary to maintain a realistic global DFe inventory (Tables 1 and 2). Scavenging is thus more effective at reducing DFe concentrations in the high source flux simulations. In regions far away from the source fluxes, particularly in the deep ocean (Figure 2) and open ocean (e.g. see Figure 5e-h, Figure 6a,b), the model simulations with higher source fluxes actually contain lower dFe because the enhanced scavenging outweighs the source fluxes in these areas. Lower DFe concentrations in these deep and open ocean regions better reproduce observations further improving the model-data misfit metrics (Figure 7).

4 Discussion

4.1 Model-Data Constraints and Uncertainties

The variable ligand parameterization significantly improved the model's ability to reproduce the distribution of DFe observations in the interior ocean mainly due to AOU dependency of this parameterization. Since ligands are produced when dissolved oxygen is consumed during the respiration of POM via heterotrophic microbes in the variable ligand parameterization, their concentrations reach maximum values in old Pacific intermediate waters (Figure 3), which prevents scavenging causing the model to better reproduce high observed DFe concentrations there (Figure 4h). This model improvement suggests that ligand production by heterotrophic bacteria is a key mechanism maintaining the global marine iron cycle (Misumi et al., 2013;Pham and Ito, 2018).

Although not a focus of this study, the model was not able to reproduce the full spatial extent of high DFe concentrations near hydrothermal vents at mid-ocean depths (Figure 4) despite that this source is included (Table 2). Resing et al. (2015) was only able to reproduce this DFe extent when assuming that the hydrothermal vents were also a significant source of ligands. This emphasizes that future model versions should include ligands as prognostic tracers to more mechanistically represent their importance in marine iron models, but that a more robust global

342 database of ligand concentrations including their binding strength would be required (Völker and
343 Tagliabue, 2015).

344 The ligand and high sedimentary DFe release effects have similar spatial impacts on DFe
345 concentrations making it difficult to constrain their individual impacts with DFe concentrations
346 alone. This spatial overlap is most pronounced near ODZs in the eastern tropical Pacific, eastern
347 tropical Atlantic, and Northern Indian Ocean. This spatial covariance occurs because when AOU
348 is high, bottom water oxygen is typically low. Therefore, DFe concentrations are enhanced both
349 by reduced scavenging due to high ligands where AOU is high as well as high sedimentary DFe
350 release rates where bottom water oxygen is low. Future studies should examine the integrative
351 DFe cycling in these systems (e.g. sedimentary release rates and ligand concentrations) to give
352 additional insights on individual processes contributions to total DFe.

353 Despite high sedimentary release rates, the *SedFeHigh* model simulations still
354 underestimate DFe on most continental shelf systems. The poorly resolved coastal dynamics in
355 our coarse resolution circulation model is likely a key model deficiency preventing the model
356 from representing many coastal dynamics where sedimentary DFe fluxes are high. Coarse
357 resolution models underestimate coastal upwelling and the nutrient input on narrow shelf
358 systems that drive productivity. This bias causes underestimated particulate organic matter
359 production as well as overestimated dissolved bottom water oxygen concentrations, both of
360 which would contribute to underestimating reductive sedimentary DFe release rates and from
361 coastal shelf systems.

362 Further complicating matters are interactions between sedimentary DFe release fluxes,
363 ligands, and scavenging. For example, our *SedFeHigh* model simulation releases significantly
364 higher DFe on high latitude shelves (Figure 2e-f). However, only a small part of this DFe
365 remains in the dissolved pool since scavenging efficiently converts it to particulate iron that
366 eventually sinks back to the sediments. Therefore, our model underestimation of DFe
367 concentrations remains despite high DFe release rates. Underestimated organic matter due to
368 nutrient upwelling or the exclusion of riverine inputs which may include ligands could also
369 contribute to this model bias. If our ligand parameterization predicted higher concentrations on
370 these high latitude shelf systems, which has been indicated by ligand observations (Völker and

Tagliabue, 2015), this would prevent rapid scavenging of DFe released from sediments and better reproduce observations.

Sedimentary DFe release rates may still be underestimated even in our high release scenario. Note that our highest tested global sedimentary release rate (117 Gmol yr^{-1}) was not the highest from the marine iron mode intercomparison (up to 194 Gmol yr^{-1}) (Tagliabue et al., 2016), and every model scenario tested here with increased source fluxes improved the model-data misfit metrics (Figure 7). One potentially important process not included in the model is non-reductive dissolution from young, tectonically active sediments (Conway and John, 2014;Homoky et al., 2013), which could further contribute to higher total sedimentary DFe release rates that may improve the model.

An important limitation of applying these empirical functions of sedimentary DFe release (e.g. (Dale et al., 2015;Elrod et al., 2004)) in global models is that total iron balance within the sediments is not explicitly accounted for. Thus, these parameterizations can potentially represent an infinite source of DFe to the ocean which is unrealistic. This simplification can be justified because many important sources of particulate Fe to the sediment are not yet included in the model, e.g. atmospheric and riverine input of lithogenic material and in situ production in active margins (e.g. volcanic or subduction zones), which provide DFe for release. Also note that the Dale et al. (2015) parameterization applied in the *SedFeHigh* simulations sets a maximum rate determined under steady-state conditions which caps potentially unrealistic high release rates. While this simplification is likely not a significant deficiency in steady-state model simulations presented here, this should be considered in transient simulations with substantial enhancement of sedimentary DFe fluxes.

Atmospheric deposition often occurs at high rates over continental shelves (e.g. North Pacific, Patagonia) and ODZs (e.g. Arabian Sea), again making it difficult to constrain individual processes driving DFe concentrations when multiple processes act together in close spatial proximity. For example, our high atmospheric soluble deposition scenario helps reproduce high DFe concentrations in the Arabian Sea (Figure 5g,h). However, our model underestimates the extent of the Arabian ODZ which could be the real cause driving high DFe concentrations there via high sedimentary DFe release, reduced scavenging, and/or enhanced redox cycling (Moffett et al., 2007).

The model simulations do not resolve the high variance of the observations which is reflected in the underestimated standard deviation model-data misfit metric (i.e. normalized standard deviation values fall below the value one; Figure 7). High variance in the global dataset may not reflect mean climatological conditions simulated by the steady-state model results given the highly dynamic nature of DFe cycling particularly in the surface ocean (Black et al., 2020), and the limitations of spatial and temporal sparsity of the dataset. But note that the standard deviation was significantly improved in our best model simulation with variable ligands and high source/scavenging fluxes (#5 *Atm+SedFeHigh_LigVar*; see Figure 7). Since most DFe observations have been collected in recent decades, there could already be a significant anthropogenic impact (e.g. enhanced deoxygenation, atmospheric pollutant deposition) on the global marine iron cycle not included in these model simulations, especially if the marine DFe residence time operates on decadal timescales or less. Future additions and expansion to the global DFe dataset as well as comparison with transient model simulations at the same period of data collection will improve uncertainties in future model-data analyses.

4.2 A global marine iron cycle with a mean residence time under a decade?

Our model simulations testing various external source fluxes in the global marine iron cycle result in global average residence times ranging from 7.5 to 36 years. The simulation that best reproduces the observations (#5 *Atm+SedFeHigh_LigVar*) has the lowest residence time (global: 7.5 years; surface ocean: 0.83 years) among our model experiments. This low-end residence time is caused in large part due to the high source fluxes, with the reductive sedimentary release being the most important with the highest rate in our simulations. These high source fluxes need to be compensated by efficient scavenging and subsequent removal via burial in the sediments to reproduce the distribution and global mean inventory in DFe observations.

This is in general agreement with observational studies focusing on the surface layer (Black et al., 2020;Sarthou et al., 2003). For example, Black et al. (2020) estimated similar residence times throughout the global surface ocean (0-250 meters) for DFe ranging from approximately 1 month to 4 years depending on the region and specific iron pools considered, although noting that the uncertainties remain large (i.e. equal or greater than the absolute value of the estimate in each region). These generally low surface residence times are captured in our model simulations that range from 0.83 to 3.12 years (Table 2). Whereas DFe in the ocean

interior is more stable and controlled by the amount of ligands that prevent scavenging and removal to the sediments via sinking particulates, contributing to the longer global mean residence times.

4.3 Marine iron flux impacts on global ocean biogeochemistry

An interesting feature of the model simulations is that there is surprisingly little change to large scale marine productivity, export production, and ODZ volume (Table 3). This occurs in large part in the model because scavenging was also increased in high sedimentary iron release scenarios, and thus much of the additional DFe fluxes from the sediments is efficiently scavenged to particulate iron that sinks back to the sediments before it can be transported to the surface ocean where it may stimulate additional productivity. This general impact was also found in a model study using a previous iteration of the model version used here but comparing different complexities of the marine iron configurations (Yao et al., 2019) rather than source and scavenging fluxes tested here.

However, there was a notable increase in dissolved oxygen levels originating in the Southern Ocean among our model simulations (Table 3). The variable ligand parameterization predicts less ligands in the Southern Ocean (Figure 3), which allows higher scavenging to reduce DFe that better reproduces observations. Furthermore, since external iron sources in the Southern Ocean are small (Figure 2,4j), the enhanced scavenging in the high source flux simulations removes more DFe than source fluxes add to the Southern Ocean. Therefore, DFe levels further decrease in the Southern Ocean (Figure 4k, 5e-h) in the high source flux scenarios. The high scavenging in our best model simulation with variable ligands and high source fluxes (#5 *Atm+SedFeHigh_LigVar*) reduces DFe, marine productivity and resulting oxygen consumption during remineralization of particulate organic matter, thereby increasing dissolved oxygen concentrations at depth. This effect is significant enough to increase average global dissolved oxygen concentrations by 8% in the model because water masses formed in the Southern Ocean contribute to much of the global deep ocean (Table 3). This emphasizes the importance of simulating a robust global marine iron cycle most importantly in the Southern Ocean.

5 Conclusions

In this study we tested various rates of atmospheric soluble deposition, reductive sedimentary release, and variable ligand distributions within a marine iron component in a global ocean biogeochemical model. The simulations that best reproduce the global DFe observations include highest tested source fluxes and a variable ligand parameterization. The most striking feature in the global DFe observations that supports this hypothesis is the strong gradients that often occur with high concentrations near source fluxes and low concentrations in adjacent open ocean regions. This high source flux/scavenging iron cycling regime causes a relatively short mean residence times of less than a decade in the global oceans and less than a year in the surface ocean. The short residence time implies that the global marine iron cycle is highly sensitive to environmental perturbations in the Anthropocene and geological past. Although uncertainties remain high due to model parameterizations of complex, poorly understood processes and the sparsity of DFe measurements throughout the global ocean, our model-data analysis suggests the marine iron cycle operates with relatively high source fluxes and high scavenging rates.

Acknowledgments, Samples, and Data

This study was supported by the Cluster of Excellence “The Future Ocean” from the Deutsche Forschungsgemeinschaft (DFG) and COMFORT project from the European Union Horizon 2020 program. We thank Christoph Völker for helpful comments and suggestions. We acknowledge Choa Luo, Natalie Mahowald and the GESAMP Working Group 38 for making their atmospheric deposition fields available. Model output will be made publicly accessible at GEOMAR open access repository (thredds.geomar.de).

480 **Table 1. Marine Iron Model Configurations**

#	Simulation Name	Atmospheric deposition	Sedimentary release	Ligands	Inorganic Scavenging (kFe_{prp}[a])	Particle Scavenging (kFe_{org}[b])
1	SedFeLow_LigConst	Luo2008[c]	Elrod2004[d]	Constant[e]	0.0069	1.2
2	SedFeLow_LigVar	Luo2008	Elrod2004	Variable[f]	0.0052	1.5
3	SedFeMid_LigVar	Luo2008	Dale2015[g]	Variable	0.0069	2.2
4	SedFeHigh_LigVar	Luo2008	Dale2015[h]	Variable	0.0081	2.9
5	Atm+SedFeHigh_LigVar	Myrio2018[i]	Dale2015	Variable	0.0098	2.9

481

482 a Inorganic scavenging parameter has units of d^{-1}

483 b Particle scavenging parameter has units of $(gC/m^3)^{-0.58}\ d^{-1}$

484 c (Luo et al., 2008)

485 d (Elrod et al., 2004)

486 e Constant concentration of 1 nM everywhere in the ocean

487 f Variable ligand parameterization (see section 2.3.3)

488 g Dale et al. (2015) function with reduced maximum flux rate 100 μmol $m^{-2}\ d^{-1}$

489 h Dale et al. (2015) function with suggested maximum flux rate 170 μmol $m^{-2}\ d^{-1}$

490 i (Myriokefalitakis et al., 2018)

Table 2. Global Marine Iron Cycle Results

#	Simulation Name	Atmospheric soluble deposition (Gmol yr^{-1})	Reductive Sedimentary release (Gmol yr^{-1})	Hydro-thermal (Gmol yr^{-1})	Inorganic Scavenging (Gmol yr^{-1})	Particle Scavenging (Gmol yr^{-1})	Dissolved Iron (nM)	Global Residence time[a] (yr)	Surface Residence time[b] (yr)
1	SedFeLow_LigConst	1.4	15.1	11.4	34.3	22.5	0.68	33.3	3.12
2	SedFeLow_LigVar	1.4	14.6	11.4	30.9	29.3	0.73	35.9	2.56
3	SedFeMid_LigVar	1.4	68.6	11.4	99.3	55.9	0.73	12.2	1.35
4	SedFeHigh_LigVar	1.4	117	11.4	159	83.9	0.73	7.66	0.87
5	Atm+SedFeHigh_LigVar	3.4	114	11.4	162	81.5	0.71	7.49	0.83

[a]Since our iron model simulates active (re)cycling between particulates and dissolved forms and thus scavenging does not permanently remove bioavailable iron from the system, we calculate residence time based on external fluxes of this global system, i.e. global Fe inventory/∑Source Inputs.

[b]For surface residence time, we follow Black et al. (2020) by including the upper 250 meters and account for sinking particulate iron out of this layer as the sink flux. Since our particulate iron pool includes both biogenic (i.e. produced during primary production) and authigenic (i.e. produced by scavenging) iron in the model, this model residence time is comparable to their mean dissolved, biogenic+authigenic estimate, which ranges from 0.1 to 4 years depending on location.

500 **Table 3. Global Marine Biogeochemistry Results**

#	Simulation Name	Net Primary Production (Gt C yr^{-1})	Export Production (Gt C yr^{-1})	Global O_2 (mmol m^{-3})	Southern Ocean O_2 (mmol m^{-3})	Suboxic Volume (x10^{15} m^3)
1	SedFeLow_LigConst	47.0	8.1	167.1	206.3	8.5
2	SedFeLow_LigVar	47.4	7.9	174.6	216.3	7.7
3	SedFeMid_LigVar	47.7	7.9	177.5	220.7	7.7
4	SedFeHigh_LigVar	48.0	7.9	178.6	222.0	7.5
5	Atm+SedFeHigh_LigVar	47.9	7.8	180.5	224.2	6.6

501

Figure 1. Schematic of the marine iron (Fe) model. See section 2.3 for a full description.

Figure 2. Vertically-integrated, annual fluxes of atmospheric soluble iron deposition (top row) prescribed on the base (BASE) model simulations from Luo et al. (2008) (a)**,** high scenario (*Atm+*) from the GESAMP intermodel average (Myriokefalitakis et al., 2018) (b), and their difference (c). Bottom row: Sedimentary iron release using functions based on Elrod et al. (2004) (*SedFeLow*) (d) and Dale et al. (2015) (*SedFeHigh*) (e), and their difference (f).

Figure 3. Distribution of variable ligand concentrations in the surface (0-250 meters) ocean (a), and basin-scale averages in the Atlantic (b), Indian (c), Pacific (d), and Southern (e). Note that the Southern Ocean sector (>40°S) was excluded from the other basins.

Figure 4. Annually averaged depth profiles of marine iron source inputs (left column), dissolved iron concentrations (center column), and scavenging rates (right column) in the Global, Atlantic, Indian-Pacific, and Southern Ocean for model simulations (colored) and dissolved iron observations (filled black circles). Source inputs (left column) are atmospheric soluble deposition as large filled symbols in the base (green squares) and high (Atm+; red diamonds) scenarios, sedimentary iron release in the low (*SedFeLow*; blue circles) and high scenarios (*SedFeHigh*; purple triangles), and hydrothermal flux (open green boxes, applied to all simulations). For dissolved iron concentrations (center column), lines show model averages in the entire selected domain, while symbols include model results only where dissolved iron observations exist. Note that the Southern Ocean sector (>40°S) is excluded from the Atlantic and Indian-Pacific basins.

Figure 5. Annually averaged dissolved iron concentrations in the upper 250 meters in observations (a), *SedFeLow_LigConst* (b), *SedFeLow_LigVar* (c), *SedFeHigh_LigVar* (e), and *Atm+SedFeHigh_LigVar* (g). Right column highlights individual effects on dissolved iron concentrations by showing model differences from variable ligands (i.e. *SedFeLow_LigVar−SedFeLow_LigConst*) (d), high sedimentary iron release (i.e. *SedFeHigh_LigVar−SedFeLow_LigVar*) (f), and high atmospheric soluble deposition (i.e. *Atm+SedFeHigh_LigVar−SedFeHigh_LigVar*) (h).

Figure 6. Comparison of dissolved iron measurements (black circles) in the upper 250 meters with model simulations *SedFeLow_LigConst* (green squares), *SedFeLow_LigVar* (blue circles), *SedFeHigh_LigVar* (purple triangles), *Atm+SedFeHigh_LigVar* (red diamonds) across ocean basin sections in the tropical Pacific (meridional average from 20°S-20°N) (a); central Pacific (zonal averaged from 180°-150°W) (b); Indian (zonal averaged from 20°-100°E) (c); and eastern Atlantic (zonal averaged from 20°W-15°E) (d). Lines show model averages in the entire selected domain, while symbols include model results only at locations where observations exist. Since the core of oxygen deficient zones in the model does not overlap with the real ocean where high dissolved iron concentrations exist in the eastern Pacific (a) and northern Indian (c), we added dissolved iron concentrations directly above the core of the oxygen deficient zones ($O_2 < 5$ mmol m^{-3}) in the model as star symbols.

Figure 7. Model-data statistical metrics calculated using all observations (upper panels a-f) and using only GEOTRACES observations (lower panels g-l). Correlation coefficient (left column), standard deviation (center column), root-mean-squared error (right column) are calculated for the global ocean (top rows) and upper 250 meters of the water column (bottom rows). Standard deviation (b,e) and root-mean-squared error (c,f) are normalized by the standard deviation of observations. Note that vertical axes have been adjusted to show the full range in each individual panel.

References

Anderson, R. F., Cheng, H., Edwards, R. L., Fleisher, M. Q., Hayes, C. T., Huang, K. F., Kadko, D., Lam, P. J., Landing, W. M., Lao, Y., Lu, Y., Measures, C. I., Moran, S. B., Morton, P. L., Ohnemus, D. C., Robinson, L. F., and Shelley, R. U.: How well can we quantify dust deposition to the ocean?, Philos Trans A Math Phys Eng Sci, 374, 10.1098/rsta.2015.0285, 2016.

Aumont, O., Ethé, C., Tagliabue, A., Bopp, L., and Gehlen, M.: PISCES-v2: an ocean biogeochemical model for carbon and ecosystem studies, Geoscientific Model Development, 8, 2465-2513, 10.5194/gmd-8-2465-2015, 2015.

Black, E. E., Kienast, S. S., Lemaitre, N., Lam, P. J., Anderson, R. F., Planquette, H., Planchon, F., and Buesseler, K. O.: Ironing Out Fe Residence Time in the Dynamic Upper Ocean, Global Biogeochemical Cycles, 34, 10.1029/2020gb006592, 2020.

Boyd, P. W., and Ellwood, M. J.: The biogeochemical cycle of iron in the ocean, Nature Geoscience, 3, 675-682, 10.1038/ngeo964, 2010.

Bruland, K. W., Middag, R., and Lohan, M. C.: 8.2 - Controls of Trace Metals in Seawater, in: Treatise on Geochemistry (Second Edition), edited by: Holland, H. D., and Turekian, K. K., Elsevier, Oxford, 19-51, 2014.

Bundy, R. M., Boiteau, R. M., McLean, C., Turk-Kubo, K. A., McIlvin, M. R., Saito, M. A., Van Mooy, B. A. S., and Repeta, D. J.: Distinct Siderophores Contribute to Iron Cycling in the Mesopelagic at Station ALOHA, Frontiers in Marine Science, 5, 10.3389/fmars.2018.00061, 2018.

Conway, T. M., and John, S. G.: Quantification of dissolved iron sources to the North Atlantic Ocean, Nature, 511, 212-215, 10.1038/nature13482, 2014.

Croot, P. L., Streu, P., and Baker, A. R.: Short residence time for iron in surface seawater impacted by atmospheric dry deposition from Saharan dust events, Geophysical Research Letters, 31, 10.1029/2004gl020153, 2004.

Dale, A. W., Nickelsen, L., Scholz, F., Hensen, C., Oschlies, A., and Wallmann, K.: A revised global estimate of dissolved iron fluxes from marine sediments, Global Biogeochemical Cycles, 29, 691-707, 10.1002/2014gb005017, 2015.

Eby, M., Zickfeld, K., Montenegro, A., Archer, D., Meissner, K. J., and Weaver, A. J.: Lifetime of Anthropogenic Climate Change: Millennial Time Scales of Potential CO2 and Surface Temperature Perturbations, Journal of Climate, 22, 2501-2511, 10.1175/2008jcli2554.1, 2009.

Elrod, V. A., Berelson, W. M., Coale, K. H., and Johnson, K. S.: The flux of iron from continental shelf sediments: A missing source for global budgets, Geophysical Research Letters, 31, L12307, 10.1029/2004gl020216, 2004.

Frants, M., Holzer, M., DeVries, T., and Matear, R.: Constraints on the global marine iron cycle from a simple inverse model, Journal of Geophysical Research: Biogeosciences, 121, 28-51, 10.1002/2015jg003111, 2016.

Galbraith, E. D., Gnanadesikan, A., Dunne, J. P., and Hiscock, M. R.: Regional impacts of iron-light colimitation in a global biogeochemical model, Biogeosciences, 7, 1043-1064, 10.5194/bg-7-1043-2010, 2010.

Gent, P. R., and McWilliams, J. C.: Isopycnal Mixing in Ocean Circulation Models, Journal of Physical Oceanography, 20, 150-155, doi:10.1175/1520-0485(1990)020<0150:IMIOCM>2.0.CO;2, 1990.

597 Getzlaff, J., and Dietze, H.: Effects of increased isopycnal diffusivity mimicking the unresolved
598 equatorial intermediate current system in an earth system climate model, Geophysical
599 Research Letters, 10.1002/grl.50419, 2013.
600 Gledhill, M., and Buck, K. N.: The organic complexation of iron in the marine environment: a
601 review, Frontiers in microbiology, 3, 10.3389/fmicb.2012.00069, 2012.
602 Homoky, W. B., John, S. G., Conway, T. M., and Mills, R. A.: Distinct iron isotopic signatures
603 and supply from marine sediment dissolution, Nat Commun, 4, 2143,
604 10.1038/ncomms3143, 2013.
605 Honeyman, B. D., Balistrieri, L. S., and Murray, J. W.: Oceanic trace metal scavenging: the
606 importance of particle concentration, Deep Sea Research Part A. Oceanographic
607 Research Papers, 35, 227-246, https://doi.org/10.1016/0198-0149(88)90038-6, 1988.
608 Johnson, K. S., Gordon, R. M., and Coale, K. H.: What controls dissolved iron concentrations in
609 the world ocean?, Marine Chemistry, 57, 137-161, https://doi.org/10.1016/S0304-
610 4203(97)00043-1, 1997.
611 Kalnay, E., Kanamitsu, M., Kistler, R., Collins, W., Deaven, D., Gandin, L., Iredell, M., Saha,
612 S., White, G., Woollen, J., Zhu, Y., Leetmaa, A., Reynolds, R., Chelliah, M., Ebisuzaki,
613 W., Higgins, W., Janowiak, J., Mo, K. C., Ropelewski, C., Wang, J., Jenne, R., and
614 Joseph, D.: The NCEP/NCAR 40-Year Reanalysis Project, Bulletin of the American
615 Meteorological Society, 77, 437-471, 10.1175/1520-
616 0477(1996)077<0437:tnyrp>2.0.co;2, 1996.
617 Kvale, K. F., Meissner, K. J., Keller, D. P., Eby, M., and Schmittner, A.: Explicit Planktic
618 Calcifiers in the University of Victoria Earth System Climate Model, Version 2.9,
619 Atmosphere-Ocean, 53, 332-350, 10.1080/07055900.2015.1049112, 2015.
620 Large, W. G., Danabasoglu, G., McWilliams, J. C., Gent, P. R., and Bryan, F. O.: Equatorial
621 Circulation of a Global Ocean Climate Model with Anisotropic Horizontal Viscosity,
622 Journal of Physical Oceanography, 31, 518-536, doi:10.1175/1520-
623 0485(2001)031<0518:ECOAGO>2.0.CO;2, 2001.
624 Luo, C., Mahowald, N., Bond, T., Chuang, P. Y., Artaxo, P., Siefert, R., Chen, Y., and Schauer,
625 J.: Combustion iron distribution and deposition, Global Biogeochemical Cycles, 22,
626 GB1012, 10.1029/2007gb002964, 2008.
627 Misumi, K., Lindsay, K., Moore, J. K., Doney, S. C., Tsumune, D., and Yoshida, Y.: Humic
628 substances may control dissolved iron distributions in the global ocean: Implications
629 from numerical simulations, Global Biogeochemical Cycles, 27, 450-462,
630 10.1002/gbc.20039, 2013.
631 Moffett, J. W., Goepfert, T. J., and Naqvi, S. W. A.: Reduced iron associated with secondary
632 nitrite maxima in the Arabian Sea, Deep Sea Research Part I: Oceanographic Research
633 Papers, 54, 1341-1349, 10.1016/j.dsr.2007.04.004, 2007.
634 Moore, C. M., Mills, M. M., Arrigo, K. R., Berman-Frank, I., Bopp, L., Boyd, P. W., Galbraith,
635 E. D., Geider, R. J., Guieu, C., Jaccard, S. L., Jickells, T. D., La Roche, J., Lenton, T. M.,
636 Mahowald, N. M., Marañón, E., Marinov, I., Moore, J. K., Nakatsuka, T., Oschlies, A.,
637 Saito, M. A., Thingstad, T. F., Tsuda, A., and Ulloa, O.: Processes and patterns of
638 oceanic nutrient limitation, Nature Geoscience, 6, 701-710, 10.1038/ngeo1765, 2013.
639 Moore, J. K., and Braucher, O.: Sedimentary and mineral dust sources of dissolved iron to the
640 world ocean, Biogeosciences, 5, 631-656, 10.5194/bg-5-631-2008, 2008.

641 Muglia, J., Somes, C. J., Nickelsen, L., and Schmittner, A.: Combined Effects of Atmospheric
642 and Seafloor Iron Fluxes to the Glacial Ocean, Paleoceanography, 32, 1204-1218,
643 10.1002/2016pa003077, 2017.
644 Myriokefalitakis, S., Ito, A., Kanakidou, M., Nenes, A., Krol, M. C., Mahowald, N. M., Scanza,
645 R. A., Hamilton, D. S., Johnson, M. S., Meskhidze, N., Kok, J. F., Guieu, C., Baker, A.
646 R., Jickells, T. D., Sarin, M. M., Bikkina, S., Shelley, R., Bowie, A., Perron, M. M. G.,
647 and Duce, R. A.: Reviews and syntheses: the GESAMP atmospheric iron deposition
648 model intercomparison study, Biogeosciences, 15, 6659-6684, 10.5194/bg-15-6659-2018,
649 2018.
650 Nickelsen, L., Keller, D. P., and Oschlies, A.: A dynamic marine iron cycle module coupled to
651 the University of Victoria Earth System Model: the Kiel Marine Biogeochemical Model 2
652 for UVic 2.9, Geoscientific Model Development, 8, 1357-1381, 10.5194/gmd-8-1357-
653 2015, 2015.
654 Parekh, P., Follows, M. J., and Boyle, E.: Modeling the global ocean iron cycle, Global
655 Biogeochemical Cycles, 18, n/a-n/a, 10.1029/2003gb002061, 2004.
656 Peltier, W. R.: Global glacial isostacy and the surface of the ice-age Earth: The ICE-5G (VM2)
657 model and GRACE, Annual Review of Earth and Planetary Sciences, 32, 111-149,
658 10.1146/annurev.earth.32.082503.144359, 2004.
659 Pham, A. L. D., and Ito, T.: Formation and Maintenance of the GEOTRACES Subsurface-
660 Dissolved Iron Maxima in an Ocean Biogeochemistry Model, Global Biogeochemical
661 Cycles, 32, 932-953, 10.1029/2017gb005852, 2018.
662 Pham, A. L. D., and Ito, T.: Ligand Binding Strength Explains the Distribution of Iron in the
663 North Atlantic Ocean, Geophysical Research Letters, 10.1029/2019gl083319, 2019.
664 Resing, J. A., Sedwick, P. N., German, C. R., Jenkins, W. J., Moffett, J. W., Sohst, B. M., and
665 Tagliabue, A.: Basin-scale transport of hydrothermal dissolved metals across the South
666 Pacific Ocean, Nature, 523, 200-203, 10.1038/nature14577, 2015.
667 Sarthou, G., Baker, A. R., Blain, S., Achterberg, E. P., Boye, M., Bowie, A. R., Croot, P., Laan,
668 P., de Baar, H. J. W., Jickells, T. D., and Worsfold, P. J.: Atmospheric iron deposition
669 and sea-surface dissolved iron concentrations in the eastern Atlantic Ocean, Deep Sea
670 Research Part I: Oceanographic Research Papers, 50, 1339-1352,
671 https://doi.org/10.1016/S0967-0637(03)00126-2, 2003.
672 Schlitzer, R., Anderson, R. F., Dodas, E. M., Lohan, M., Geibert, W., Tagliabue, A., Bowie, A.,
673 Jeandel, C., Maldonado, M. T., Landing, W. M., Cockwell, D., Abadie, C., Abouchami,
674 W., Achterberg, E. P., Agather, A., Aguliar-Islas, A., van Aken, H. M., Andersen, M.,
675 Archer, C., Auro, M., de Baar, H. J., Baars, O., Baker, A. R., Bakker, K., Basak, C.,
676 Baskaran, M., Bates, N. R., Bauch, D., van Beek, P., Behrens, M. K., Black, E., Bluhm,
677 K., Bopp, L., Bouman, H., Bowman, K., Bown, J., Boyd, P., Boye, M., Boyle, E. A.,
678 Branellec, P., Bridgestock, L., Brissebrat, G., Browning, T., Bruland, K. W., Brumsack,
679 H.-J., Brzezinski, M., Buck, C. S., Buck, K. N., Buesseler, K., Bull, A., Butler, E., Cai,
680 P., Mor, P. C., Cardinal, D., Carlson, C., Carrasco, G., Casacuberta, N., Casciotti, K. L.,
681 Castrillejo, M., Chamizo, E., Chance, R., Charette, M. A., Chaves, J. E., Cheng, H.,
682 Chever, F., Christl, M., Church, T. M., Closset, I., Colman, A., Conway, T. M., Cossa,
683 D., Croot, P., Cullen, J. T., Cutter, G. A., Daniels, C., Dehairs, F., Deng, F., Dieu, H. T.,
684 Duggan, B., Dulaquais, G., Dumousseaud, C., Echegoyen-Sanz, Y., Edwards, R. L.,
685 Ellwood, M., Fahrbach, E., Fitzsimmons, J. N., Russell Flegal, A., Fleisher, M. Q., van
686 de Flierdt, T., Frank, M., Friedrich, J., Fripiat, F., Fröllje, H., Galer, S. J. G., Gamo, T.,

687 Ganeshram, R. S., Garcia-Orellana, J., Garcia-Solsona, E., Gault-Ringold, M., George,
688 E., Gerringa, L. J. A., Gilbert, M., Godoy, J. M., Goldstein, S. L., Gonzalez, S. R.,
689 Grissom, K., Hammerschmidt, C., Hartman, A., Hassler, C. S., Hathorne, E. C., Hatta,
690 M., Hawco, N., Hayes, C. T., Heimbürger, L.-E., Helgoe, J., Heller, M., Henderson, G.
691 M., Henderson, P. B., van Heuven, S., Ho, P., Horner, T. J., Hsieh, Y.-T., Huang, K.-F.,
692 Humphreys, M. P., Isshiki, K., Jacquot, J. E., Janssen, D. J., Jenkins, W. J., John, S.,
693 Jones, E. M., Jones, J. L., Kadko, D. C., Kayser, R., Kenna, T. C., Khondoker, R., Kim,
694 T., Kipp, L., Klar, J. K., Klunder, M., Kretschmer, S., Kumamoto, Y., Laan, P., Labatut,
695 M., Lacan, F., Lam, P. J., Lambelet, M., Lamborg, C. H., Le Moigne, F. A. C., Le Roy,
696 E., Lechtenfeld, O. J., Lee, J.-M., Lherminier, P., Little, S., López-Lora, M., Lu, Y.,
697 Masque, P., Mawji, E., McClain, C. R., Measures, C., Mehic, S., Barraqueta, J.-L. M.,
698 van der Merwe, P., Middag, R., Mieruch, S., Milne, A., Minami, T., Moffett, J. W.,
699 Moncoiffe, G., Moore, W. S., Morris, P. J., Morton, P. L., Nakaguchi, Y., Nakayama, N.,
700 Niedermiller, J., Nishioka, J., Nishiuchi, A., Noble, A., Obata, H., Ober, S., Ohnemus, D.
701 C., van Ooijen, J., O'Sullivan, J., Owens, S., Pahnke, K., Paul, M., Pavia, F., Pena, L. D.,
702 Peters, B., Planchon, F., Planquette, H., Pradoux, C., Puigcorbé, V., Quay, P., Queroue,
703 F., Radic, A., Rauschenberg, S., Rehkämper, M., Rember, R., Remenyi, T., Resing, J. A.,
704 Rickli, J., Rigaud, S., Rijkenberg, M. J. A., Rintoul, S., Robinson, L. F., Roca-Martí, M.,
705 Rodellas, V., Roeske, T., Rolison, J. M., Rosenberg, M., Roshan, S., Rutgers van der
706 Loeff, M. M., Ryabenko, E., Saito, M. A., Salt, L. A., Sanial, V., Sarthou, G.,
707 Schallenberg, C., Schauer, U., Scher, H., Schlosser, C., Schnetger, B., Scott, P., Sedwick,
708 P. N., Semiletov, I., Shelley, R., Sherrell, R. M., Shiller, A. M., Sigman, D. M., Singh, S.
709 K., Slagter, H. A., Slater, E., Smethie, W. M., Snaith, H., Sohrin, Y., Sohst, B., Sonke, J.
710 E., Speich, S., Steinfeldt, R., Stewart, G., Stichel, T., Stirling, C. H., Stutsman, J., Swarr,
711 G. J., Swift, J. H., Thomas, A., Thorne, K., Till, C. P., Till, R., Townsend, A. T.,
712 Townsend, E., Tuerena, R., Twining, B. S., Vance, D., Velazquez, S., Venchiarutti, C.,
713 Villa-Alfageme, M., Vivancos, S. M., Voelker, A. H. L., Wake, B., Warner, M. J.,
714 Watson, R., van Weerlee, E., Alexandra Weigand, M., Weinstein, Y., Weiss, D.,
715 Wisotzki, A., Woodward, E. M. S., Wu, J., Wu, Y., Wuttig, K., Wyatt, N., Xiang, Y.,
716 Xie, R. C., Xue, Z., Yoshikawa, H., Zhang, J., Zhang, P., Zhao, Y., Zheng, L., Zheng, X.-
717 Y., Zieringer, M., Zimmer, L. A., Ziveri, P., Zunino, P., and Zurbrick, C.: The
718 GEOTRACES Intermediate Data Product 2017, Chemical Geology, 493, 210-223,
719 https://doi.org/10.1016/j.chemgeo.2018.05.040, 2018.
720 Schmittner, A., and Egbert, G. D.: An improved parameterization of tidal mixing for ocean
721 models, Geoscientific Model Development, 7, 211-224, 10.5194/gmd-7-211-2014, 2014.
722 Schmittner, A., and Somes, C. J.: Complementary constraints from carbon (13C) and nitrogen
723 (15N) isotopes on the glacial ocean's soft-tissue biological pump, Paleoceanography, 31,
724 669-693, 10.1002/2015PA002905, 2016.
725 Somes, C., Schmittner, A., Muglia, J., and Oschlies, A.: A three-dimensional model of the
726 marine nitrogen cycle during the Last Glacial Maximum constrained by sedimentary
727 isotopes, Frontiers in Marine Science, 4, 10.3389/fmars.2017.00108, 2017.
728 Somes, C. J., Schmittner, A., Galbraith, E. D., Lehmann, M. F., Altabet, M. A., Montoya, J. P.,
729 Letelier, R. M., Mix, A. C., Bourbonnais, A., and Eby, M.: Simulating the global
730 distribution of nitrogen isotopes in the ocean, Global Biogeochem. Cycles, 24, GB4019,
731 10.1029/2009gb003767, 2010.

Somes, C. J., and Oschlies, A.: On the influence of "non-Redfield" dissolved organic nutrient dynamics on the spatial distribution of N2 fixation and the size of the marine fixed nitrogen inventory, Global Biogeochemical Cycles, 29, 973-993, 10.1002/2014GB005050, 2015.

Tagliabue, A., Bopp, L., Dutay, J.-C., Bowie, A. R., Chever, F., Jean-Baptiste, P., Bucciarelli, E., Lannuzel, D., Remenyi, T., Sarthou, G., Aumont, O., Gehlen, M., and Jeandel, C.: Hydrothermal contribution to the oceanic dissolved iron inventory, Nature Geoscience, 3, 252-256, 10.1038/ngeo818, 2010.

Tagliabue, A., and Völker, C.: Towards accounting for dissolved iron speciation in global ocean models, Biogeosciences, 8, 3025-3039, 10.5194/bg-8-3025-2011, 2011.

Tagliabue, A., Mtshali, T., Aumont, O., Bowie, A. R., Klunder, M. B., Roychoudhury, A. N., and Swart, S.: A global compilation of dissolved iron measurements: focus on distributions and processes in the Southern Ocean, Biogeosciences, 9, 2333-2349, 10.5194/bg-9-2333-2012, 2012.

Tagliabue, A., Aumont, O., DeAth, R., Dunne, J. P., Dutkiewicz, S., Galbraith, E., Misumi, K., Moore, J. K., Ridgwell, A., Sherman, E., Stock, C., Vichi, M., Völker, C., and Yool, A.: How well do global ocean biogeochemistry models simulate dissolved iron distributions?, Global Biogeochemical Cycles, 30, 149-174, 10.1002/2015gb005289, 2016.

Tagliabue, A., Bowie, A. R., Boyd, P. W., Buck, K. N., Johnson, K. S., and Saito, M. A.: The integral role of iron in ocean biogeochemistry, Nature, 543, 51-59, 10.1038/nature21058, 2017.

Völker, C., and Tagliabue, A.: Modeling organic iron-binding ligands in a three-dimensional biogeochemical ocean model, Marine Chemistry, 173, 67-77, 10.1016/j.marchem.2014.11.008, 2015.

Weaver, A. J., Eby, M., Wiebe, E. C., Bitz, C. M., Duffy, P. B., Ewen, T. L., Fanning, A. F., Holland, M. M., MacFadyen, A., Matthews, H. D., Meissner, K. J., Saenko, O., Schmittner, A., Wang, H., and Yoshimori, M.: The UVic earth system climate model: Model description, climatology, and applications to past, present and future climates, Atmosphere-Ocean, 39, 361 - 428, 2001.

Yao, W., Kvale, K. F., Achterberg, E., Koeve, W., and Oschlies, A.: Hierarchy of calibrated global models reveals improved distributions and fluxes of biogeochemical tracers in models with explicit representation of iron, Environmental Research Letters, 14, 114009, 10.1088/1748-9326/ab4c52, 2019.

Ye, Y., and Völker, C.: On the Role of Dust-Deposited Lithogenic Particles for Iron Cycling in the Tropical and Subtropical Atlantic, Global Biogeochemical Cycles, 31, 1543-1558, 10.1002/2017gb005663, 2017.

771 Figure 1

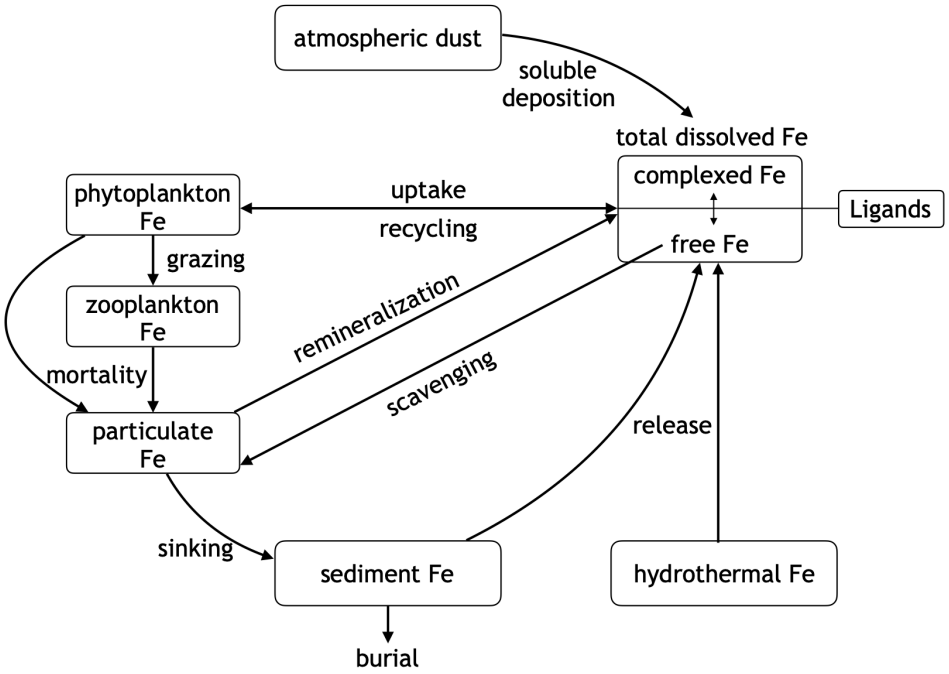

772 **Figure 1.** Schematic of the marine iron (Fe) model. See section 2.3 for a full description.

773 Figure 2

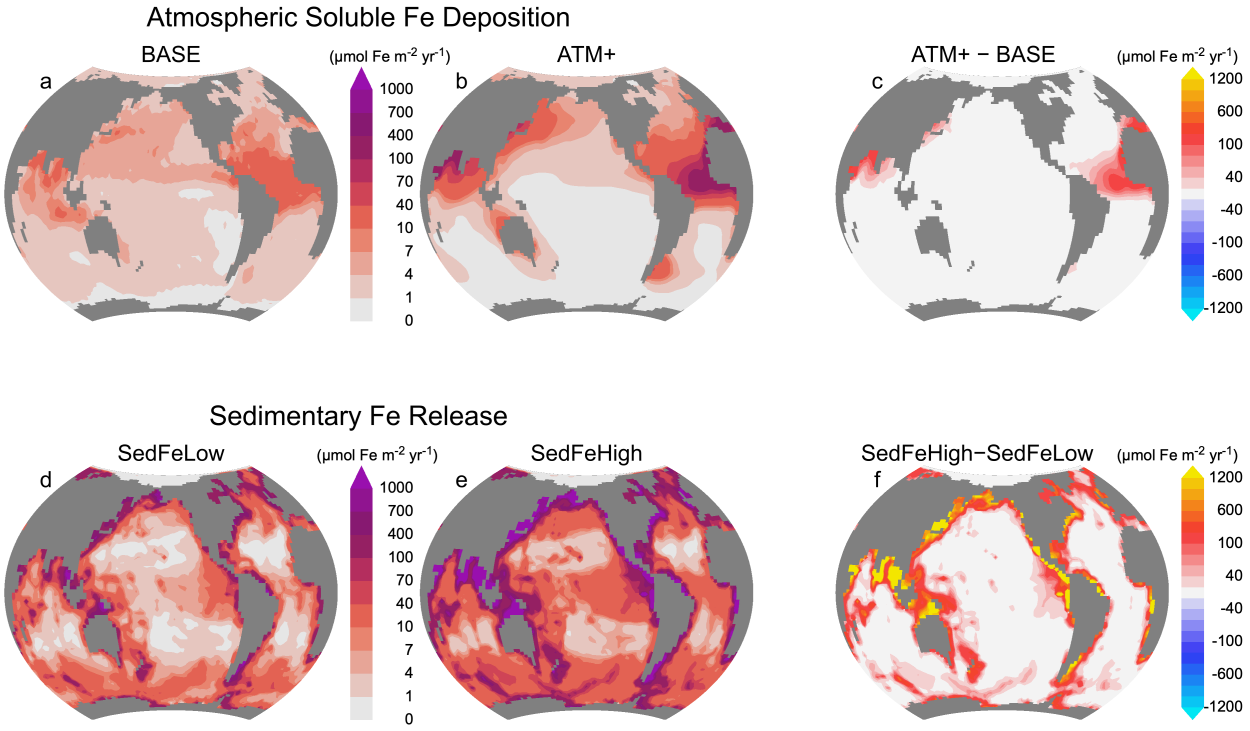

774 **Figure 2.** Vertically-integrated, annual fluxes of atmospheric soluble iron deposition (top row)
775 prescribed on the base (BASE) model simulations from Luo et al. (2008) (a), high scenario
776 (*Atm+*) from the GESAMP intermodel average (Myriokefalitakis et al., 2018) (b), and their
777 difference (c). Bottom row: Sedimentary iron release using functions based on Elrod et al.
778 (2004) (*SedFeLow*) (d) and Dale et al. (2015) (*SedFeHigh*) (e), and their difference (f).

779 Figure 3

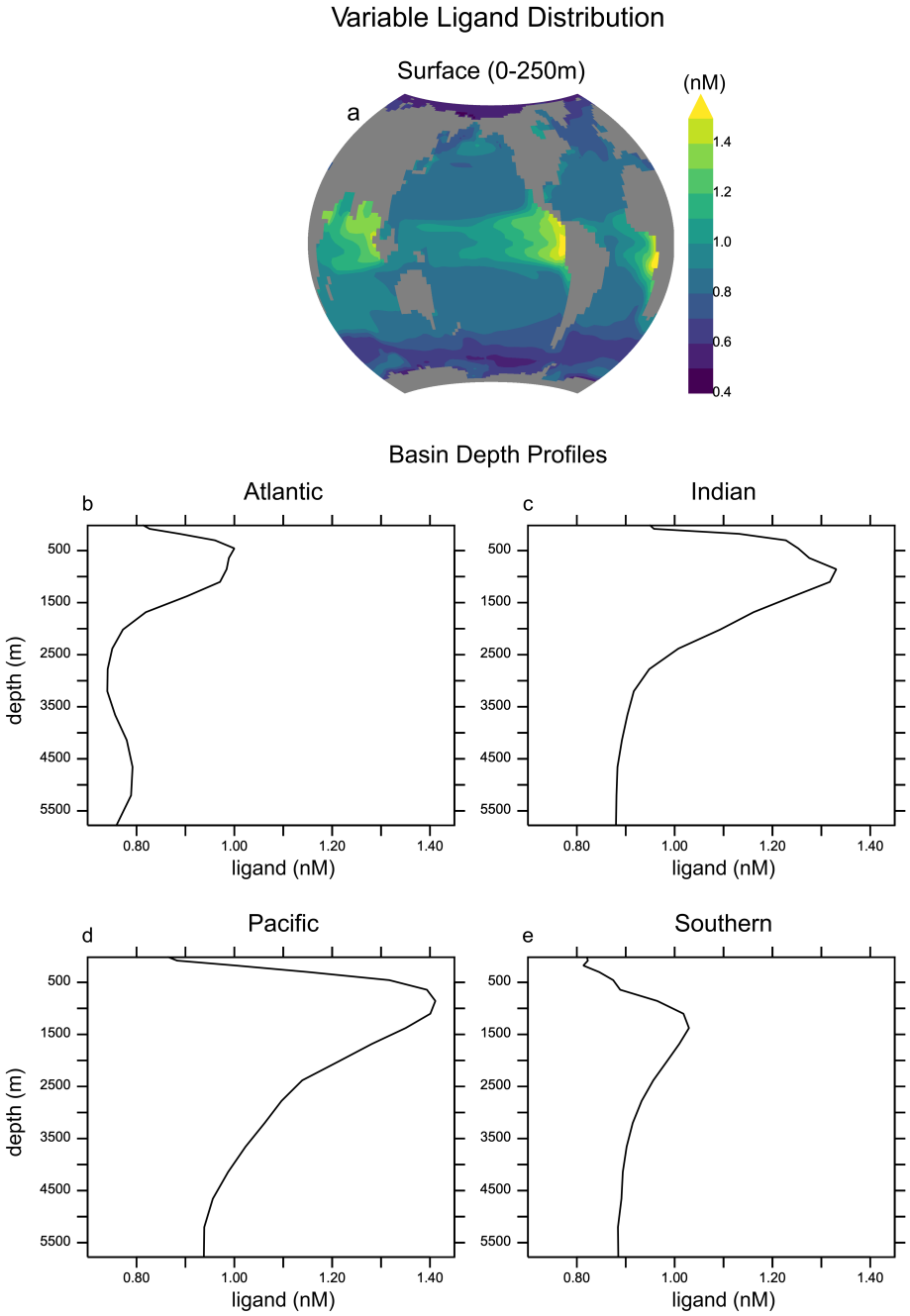

780
781 **Figure 3**. Distribution of variable ligand concentrations in the surface (0-250 meters) ocean (a),
782 and basin-scale averages in the Atlantic (b), Indian (c), Pacific (d), and Southern (e). Note that
783 the Southern Ocean sector (>40°S) was excluded from the other basins.

784 Figure 4

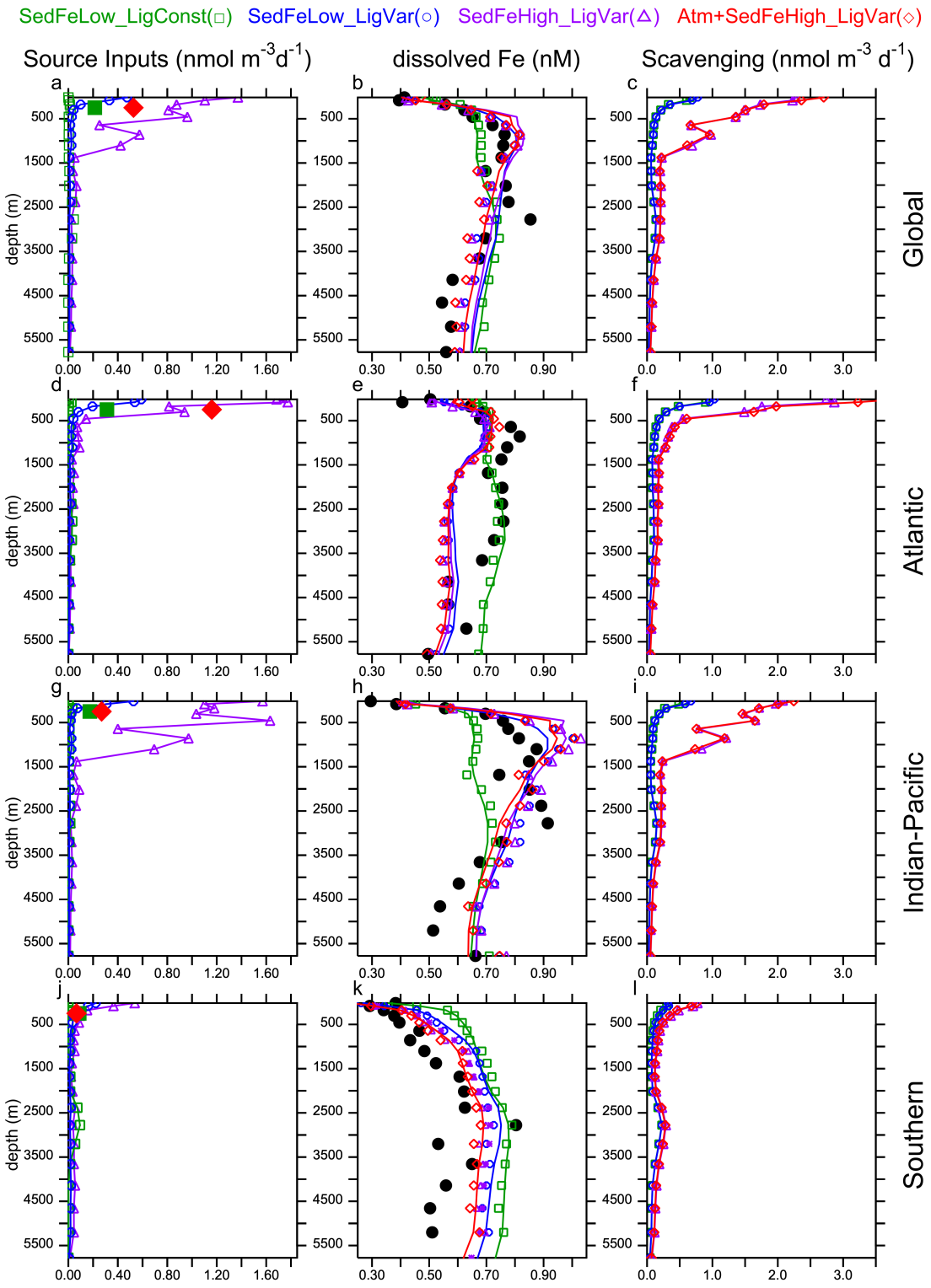
SedFeLow_LigConst(□) SedFeLow_LigVar(○) SedFeHigh_LigVar(△) Atm+SedFeHigh_LigVar(◇)
Source Inputs (nmol m-3d-1)
dissolved Fe (nM)
Scavenging (nmol m-3 d-1)
depth (m)
Global
Atlantic
Indian-Pacific
Southern

Figure 4. Annually averaged depth profiles of marine iron source inputs (left column), dissolved iron concentrations (center column), and scavenging rates (right column) in the Global, Atlantic, Indian-Pacific, and Southern Ocean for model simulations (colored) and dissolved iron observations (filled black circles). Source inputs (left column) are atmospheric soluble deposition as large filled symbols in the base (green squares) and high (Atm+; red diamonds) scenarios, sedimentary iron release in the low (*SedFeLow*; blue circles) and high scenarios (*SedFeHigh*; purple triangles), and hydrothermal flux (open green boxes, applied to all simulations). For dissolved iron concentrations (center column), lines show model averages in the entire selected domain, while symbols include model results only where dissolved iron observations exist. Note that the Southern Ocean sector (>40°S) is excluded from the Atlantic and Indian-Pacific basins.

795 Figure 5.

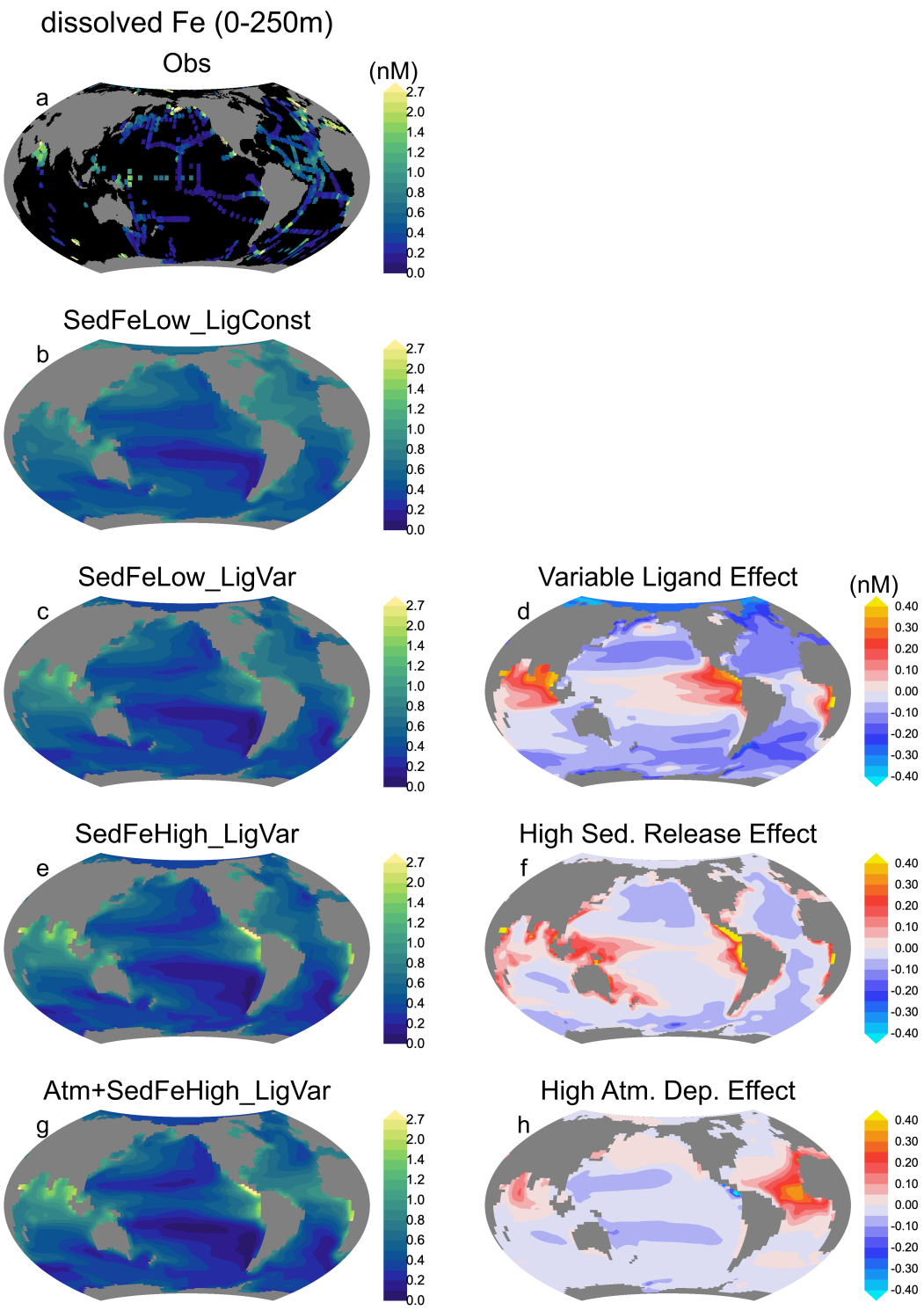

796

797 **Figure 5**. Annually averaged dissolved iron concentrations in the upper 250 meters in
798 observations (a), *SedFeLow_LigConst* (b), *SedFeLow_LigVar* (c), *SedFeHigh_LigVar* (e), and
799 *Atm+SedFeHigh_LigVar* (g). Right column highlights individual effects on dissolved iron
800 concentrations by showing model differences from variable ligands (i.e.
801 *SedFeLow_LigVar−SedFeLow_LigConst*) (d), high sedimentary iron release (i.e.
802 *SedFeHigh_LigVar−SedFeLow_LigVar*) (f), and high atmospheric soluble deposition (i.e.
803 *Atm+SedFeHigh_LigVar−SedFeHigh_LigVar*) (h).

804 Figure 6

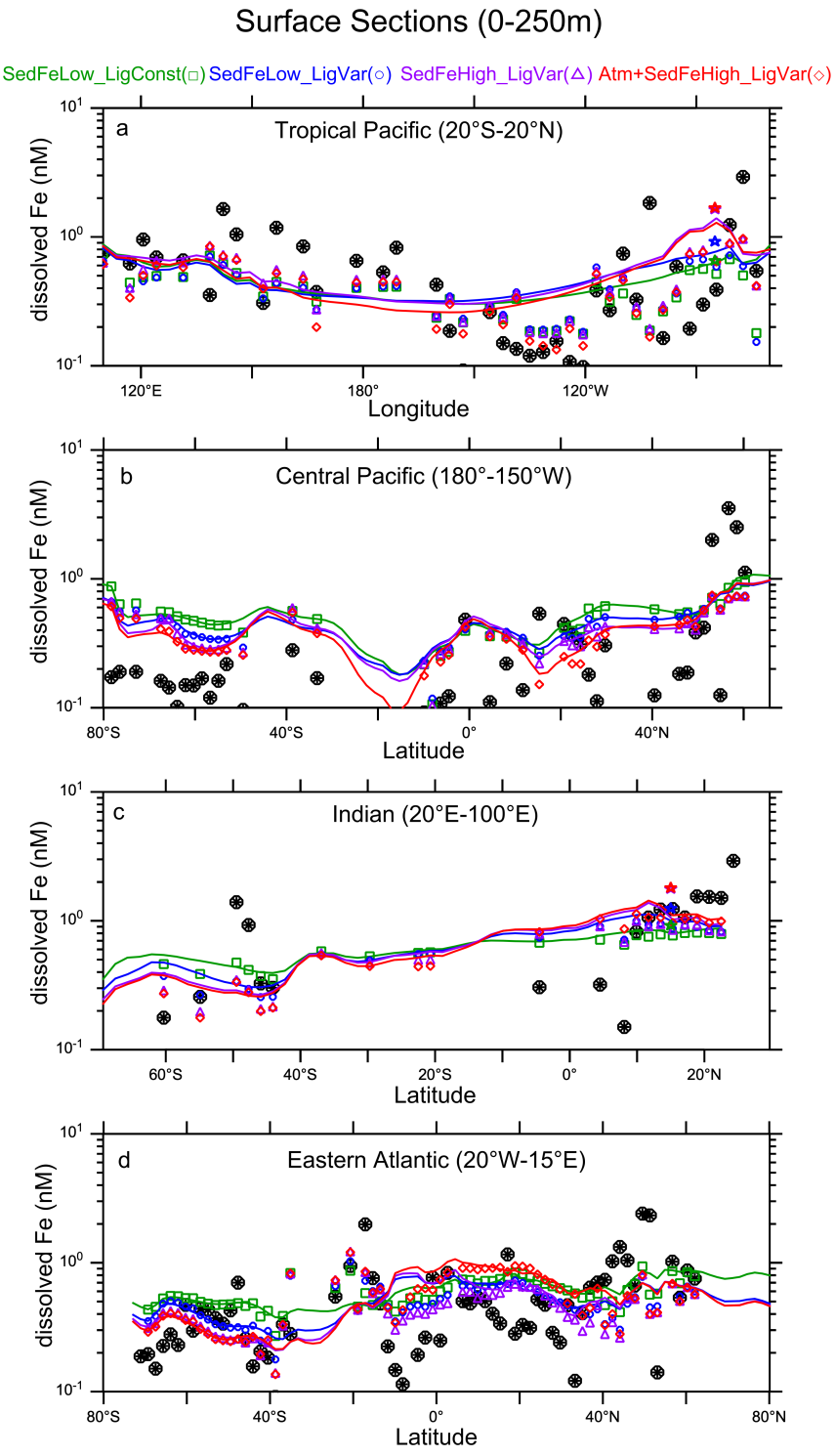

805

Figure 6. Comparison of dissolved iron measurements (black circles) in the upper 250 meters with model simulations *SedFeLow_LigConst* (green squares), *SedFeLow_LigVar* (blue circles), *SedFeHigh_LigVar* (purple triangles), *Atm+SedFeHigh_LigVar* (red diamonds) across ocean basin sections in the tropical Pacific (meridional average from 20°S-20°N) (a); central Pacific (zonal averaged from 180°-150°W) (b); Indian (zonal averaged from 20°-100°E) (c); and eastern Atlantic (zonal averaged from 20°W-15°E) (d). Lines show model averages in the entire selected domain, while symbols include model results only at locations where observations exist. Since the core of oxygen deficient zones in the model does not overlap with the real ocean where high dissolved iron concentrations exist in the eastern Pacific (a) and northern Indian (c), we added dissolved iron concentrations directly above the core of the oxygen deficient zones ($O_2 < 5$ mmol m^{-3}) in the model as star symbols.

817 Figure 7

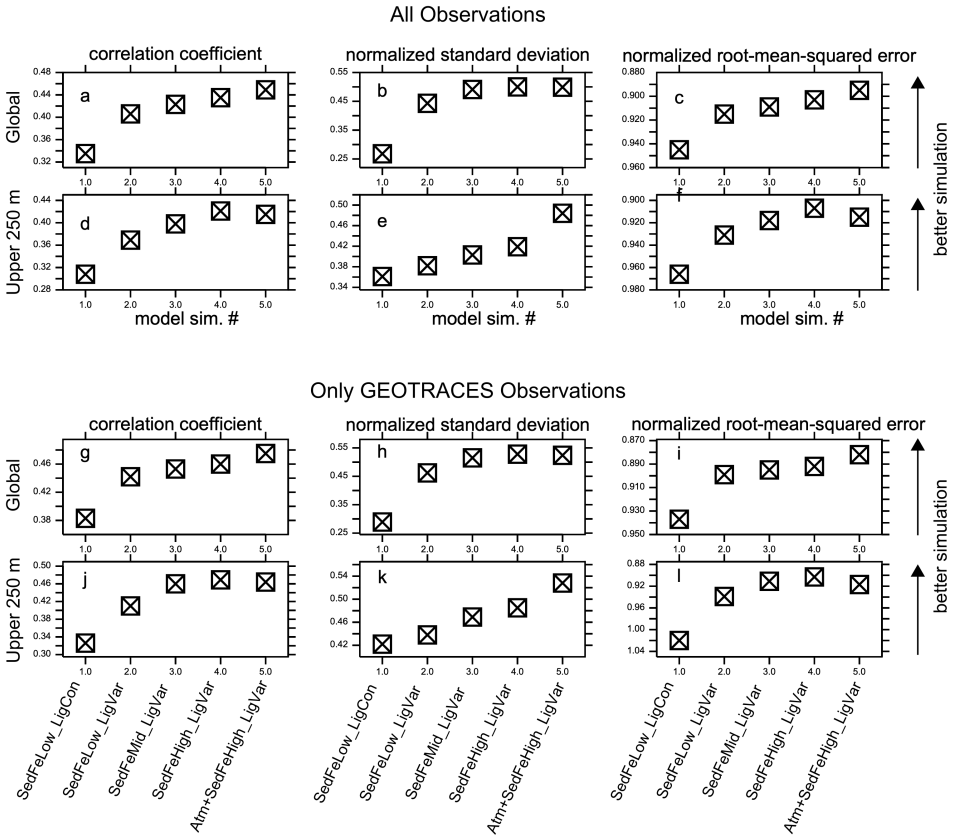

818

819 **Figure 7.** Model-data statistical metrics calculated using all observations (upper panels a-f) and
820 using only GEOTRACES observations (lower panels g-l). Correlation coefficient (left column),
821 standard deviation (center column), root-mean-squared error (right column) are calculated for the
822 global ocean (top rows) and upper 250 meters of the water column (bottom rows). Standard
823 deviation (b,e) and root-mean-squared error (c,f) are normalized by the standard deviation of
824 observations. Note that vertical axes have been adjusted to show the full range in each individual
825 panel.